J. Fluid Mech. (2009), *vol.* 618, *pp.* 155–180.
doi:10.1017/S0022112008004357 Printed in the United Kingdom

Responses of Bingham-plastic muddy seabed to a surface solitary wave

I-CHI CHAN[1] AND PHILIP L.-F. LIU[1,2]†

[1]School of Civil and Environmental Engineering, Cornell University, Ithaca, NY, USA
[2]Institute of Hydrological and Oceanic Sciences, National Central University, Jhongli, Taiwan

(Received 28 April 2008 and in revised form 7 September 2008)

In this paper, we investigate the dynamics of muddy-seabed motions induced by a surface solitary wave. The muddy seabed is characterized as Bingham-plastic mud. We focus our attention on the situations where the horizontal scale of the wave-induced mud flow is much larger than the vertical scale. The thickness of the mud layer is also assumed to be much smaller than the water depth above. With these simplifications, the dynamic pressure in the mud column remains a constant and the vertical displacement of the water–mud interface is negligible. The horizontal gradient of the wave-induced dynamic pressure along the water–seabed interface drives the motions in the mud bed. For a Bingham-plastic muddy seafloor, the mud moves either like a solid (plug flow) or like a viscous fluid (shear flow) depending on whether the magnitude of shear stress is in excess of the yield stress. Velocities inside these two different flow regimes and the location(s) of the yield surface(s) vary in time as functions of water–mud interfacial pressure gradient and the properties of the Bingham-plastic mud. A semi-analytical approach is developed in this paper to analyse the motions inside the mud bed under a surface solitary wave loading. Three possible scenarios are discussed to illustrate the complexity of the seafloor responses. The formula for the damping rate caused by the energy dissipation inside the muddy seabed is also derived. Using realistic values of the physical parameters, the present results for damping rate agree qualitatively with the available field observations.

1. Introduction

Along a muddy coast, wind waves are known to be easily damped out within a few wavelengths. Gade (1958) reported a location called the Mud Hole in the Gulf of Mexico, where the attenuation of ocean waves owing to a soft bottom is so strong that in severe weather, fishing boats frequently use it as an emergency harbour. During Hurricane Frederic in 1979, Forristall & Reece (1985) observed that off the Mississippi Delta the wave height diminished from 8.6 m to 2.5 m over a distance of 30 km. In terms of the incident wave energy, Wells & Coleman (1981) calculated from the measured wave parameters that nearly 90 % of energy was dissipated as the waves passed over the mud flat along the coast of Surinam. Elgar & Raubenheimer (2008) recorded a 70 % wave energy flux reduction when a wave propagated 1.8 km over the muddy seafloor along the Louisiana continental shelf. Similar muddy-bottom

† Email address for correspondence: pll3@cornell.edu

effects have been reported in many coasts, rivers and estuaries around the world (Healy, Wang & Healy 2002), such as the coasts along the Yellow Sea between China and Korea, the Indian Ocean coastline in South Africa, the Kerala coast of southwest India and the North Atlantic Ocean coastline in South America (Mathew, Baba & Kurian 1995; Massel 1996; Winterwerp *et al.* 2007). Mud in different locales can have different rheological behaviour, partly as a consequence of diverse chemical composition (Balmforth & Craster 2001). Because of the wide variation of seafloor properties, many constitutive models have been proposed to study mud motions driven by surface wave loadings, including the viscous fluid model (e.g. Dalrymple & Liu 1978), the viscoelastic model (e.g. MacPherson 1980) and the viscoplastic model (e.g. Mei & Liu 1987, hereinafter referred to as ML). Based on the viscosimetric tests of mud samples, Krone (1963) reported that for concentration C_w lying roughly between 10 to $100\,\mathrm{g\,L^{-1}}$, mud along the coasts of the United States displays both plastic and viscous-like behaviour, depending on the external forcing. This non-Newtonian rheology indicates that the muddy seafloor can be referred to as the Bingham-plastic material, in which the one-dimensional constitutive equations are expressed as

$$\mu_m \frac{\partial u'_m}{\partial z'} = 0, \quad |\tau'_m| \leqslant \tau'_o, \tag{1.1}$$

$$\mu_m \frac{\partial u'_m}{\partial z'} = \tau'_m - \tau'_o \mathrm{sgn}\left(\frac{\partial u'_m}{\partial z'}\right), \quad |\tau'_m| > \tau'_o, \tag{1.2}$$

where $\tau'_o > 0$ is the yield stress and μ_m represents the Bingham-plastic viscosity. Values of the physical parameters for different Bingham-plastic mud can be found in ML. Mei, Liu & Yuhi (2001) also provided useful discussions on the relationships among yield stress, Bingham-plastic viscosity, and the concentration for various types of mud.

Within the framework of linear periodic wave theory, many workers have already investigated the effects of viscous fluid mud bed (i.e. $\tau'_o = 0$) on wave propagation (e.g. Gade 1958; Dalrymple & Liu 1978; Ng 2000). Liu & Chan (2007, hereinafter referred to as LC) presented general analytical solutions for viscous mud flows under weakly nonlinear and weakly dispersive waves. They also derived a set of depth-integrated continuity and momentum equations for long-wave propagation with the viscous mud bed effects considered. They found that for a surface solitary wave loading, flow reversals occur near the bottom of the mud bed during the decelerating phase of the solitary wave. Accordingly, the mud flow velocity profile is not always parabolic in shape. Park, Liu & Clark (2008) presented a set of laboratory experiments and confirmed LC's model. Liu, Park & Cowen (2007) also demonstrated that reversed flow appears inside the water boundary layer under a surface solitary wave.

In a series of pioneering works, Mei & Liu have investigated the effects of Bingham-plastic muddy seabed on long-wave propagation and shoaling. In particular, ML examined a mud bed that is very thin compared to the height of the water column above. Consequently, the vertical motion of the water–mud interface is very small and can be ignored. Furthermore, the viscosity of water is relatively weak in comparison with that of Bingham-plastic mud and therefore, frictional stress along the water–mud

interface can also be ignored. These two assumptions were also adopted by LC in their analysis for a viscous fluid mud bed. We remark that the simplification of negligible water–mud interfacial displacement has been verified by Park *et al.* (2008). In both Bingham-plastic and viscous cases, the mud flows are driven by the wave-induced horizontal pressure gradient along the water–mud interface. Based on the constitutive equations, (1.1) and (1.2), ML illustrated elegantly that under certain approximations, the motions of Bingham-plastic muddy seafloor can be divided into two regions: a plug-flow layer moving above a shear-flow zone. The plug-flow velocity and the thickness of the shear-flow zone, or equivalently the location of the yield surface, change in time depending on the magnitude of the pressure gradient and the properties of the Bingham-plastic mud. Solutions must be obtained numerically by solving two coupled partial differential equations. In analysing the shear flow, ML applied the Kármán momentum integral method and adopted the parabolic profile to describe the horizontal velocity inside the shear-flow region. They further assumed that the plug-flow layer is always much thicker than the shear-flow zone. With these two additional simplifications, the plug-flow velocity can be obtained explicitly without knowing the shear-zone thickness, which has to be solved numerically from the deduced ordinary differential equation. Their analysis does not allow the flow reversal inside the shear-flow region as illustrated by LC for the viscous mud problem. Although the studies on purely viscous fluid problems (Liu *et al.* 2007; LC; Park *et al.* 2008) do not necessarily guarantee the same behaviour in the Bingham-plastic fluid, it is desirable to analyse the shear-flow region more carefully without using the parabolic velocity profile assumption. In addition, we anticipate that under certain combinations of yield stress, viscosity and pressure gradient, multiple shear-flow layers (or plug-flow regions) can develop.

The objective of this paper is to investigate the responses of a Bingham-plastic muddy seafloor to long water-wave loadings without some of the constraints imposed in ML. For simplicity, we shall focus only on the free-surface solitary-wave loading. In our approach, we shall relax the following two assumptions: the parabolic shear-flow velocity profile and the negligible shear-layer thickness in computing the plug-flow velocity. The relaxation of these two assumptions will allow us to investigate the evolution of yield surfaces and the associated velocity profiles throughout the entire mud column.

The paper is organized in the following manner. We first formulate the boundary-value problems governing the motions of a thin layer of Bingham-plastic mud responding to a long surface-wave loading. We then briefly review the approach and assumptions employed in ML. Relaxing some of ML's assumptions, we shall discuss several possible scenarios of mud motions, which could have up to four layers of alternating plug flow and shear flow under a surface solitary wave. After mathematically formulating these moving boundary-value problems, which are nonlinear, semi-analytical/numerical solutions are presented for the velocities inside the mud column. Detailed discussions on the mud flow dynamics with different physical parameters are presented. The damping rate for a surface solitary wave is calculated using the energy conservation law. Using some estimated but realistic physical parameters, the calculated damping rate is compared with field data. Qualitative agreement is observed.

2. Formulation

We consider a train of transient waves propagating in a constant water depth, h'_0, over a muddy seabed of thickness d'. The seabed is made of Bingham-plastic mud and the mud flow is driven by the dynamic pressure along the water–seabed interface. The wave motions are characterized by the typical wave height, a'_0, the horizontal length scale, l'_0, which is related to the magnitude of wavelength, and the time-scale, $l'_0/\sqrt{gh'_0}$. For simplicity, we shall consider only two-dimensional problems where the x'-direction coincides with the direction of wave propagation and z'_m denotes the vertical coordinate within the mud layer. Denoting (u'_m, w'_m) as the horizontal and vertical mud flow velocity components, p'_m as the dynamic pressure and τ'_m as the shear stress inside the muddy seafloor, respectively, the following dimensionless variables are introduced

$$\left.\begin{aligned} x &= x'/l'_0,\ z_m = z'_m/(\alpha l'_0),\ d = d'/(\alpha l'_0),\\ t &= t'\sqrt{gh'_0}/l'_0,\ u_m = u'_m/(\epsilon\sqrt{gh'_0}),\ w_m = w'_m/(\alpha\epsilon\sqrt{gh'_0}),\\ p_m &= p'_m/(\rho_w g a'_0),\ \tau_m = \tau'_m/(\alpha\epsilon\rho_m g h'_0), \end{aligned}\right\} \tag{2.1}$$

in which g is the acceleration due to gravity, ρ_w the water density and ρ_m the mud density. Two dimensionless parameters,

$$\epsilon = a'_0/h'_0,\quad \alpha^2 = \frac{\nu_m}{l'_0\sqrt{gh'_0}}, \tag{2.2}$$

are used in (2.1) to measure the relative importance of the nonlinearity and the viscosity, in which ν_m is the characteristic kinematic viscosity of the Bingham-plastic mud and α^2 can be viewed as the inverse of the Reynolds number.

2.1. *Boundary-layer approximation*

Following ML and LC, we assume that the muddy seabed is very thin compared with wavelength and, furthermore, the displacement of the water–mud interface is much smaller than that of the free surface, which indicates that for the present study the water–mud interface can be viewed as a horizontal line, $z_m = 0$. Hence, inside the muddy bed, the flow motion can be described by the linearized boundary-layer equations as (see LC)

$$\frac{\partial u_m}{\partial x} + \frac{\partial w_m}{\partial \eta} = 0, \quad 0 \leqslant \eta \leqslant d, \tag{2.3}$$

$$\frac{\partial u_m}{\partial t} = -\gamma\frac{\partial p_m}{\partial x} + \frac{\partial \tau_m}{\partial \eta}, \quad 0 \leqslant \eta \leqslant d, \tag{2.4}$$

in which $\eta = z_m + d$ and $\gamma = \rho_w/\rho_m$ is the density ratio. We reiterate that the dynamic pressure inside the mud bed is independent of depth because of the boundary-layer assumption.

Along the water–mud interface, the pressure is continuous. If we consider the water viscosity to be negligible, the horizontal gradient of the dynamic pressure inside the mud bed can be approximated from the horizontal momentum equation of the water column. Denoting the prescribed water–mud interfacial pressure and horizontal water velocity component as p_b and u_b, respectively, we obtain

$$\frac{\partial u_b}{\partial t} = -\frac{\partial p_b}{\partial x} = -\frac{\partial p_m}{\partial x}. \tag{2.5}$$

We should mention that p_b and u_b have the same non-dimensionalized scaling as p_m and u_m. Substituting (2.5) into (2.4), the momentum equation inside the mud bed becomes

$$\frac{\partial u_m}{\partial t} = \gamma \frac{\partial u_b}{\partial t} + \frac{\partial \tau_m}{\partial \eta} \quad (0 \leqslant \eta \leqslant d). \tag{2.6}$$

Along the water–mud interface, the tangential stress vanishes. Thus,

$$\tau_m = 0, \quad \eta = d. \tag{2.7}$$

Along the bottom of the mud bed, $\eta = 0$, the no-slip condition is imposed, i.e.

$$u_m = 0, \quad \eta = 0. \tag{2.8}$$

Once the horizontal velocity, u_m, is obtained, from the continuity equation, (2.3), the vertical velocity component can be calculated by integration as

$$w_m(x, \eta, t) = \int_0^{\eta} -\frac{\partial u_m}{\partial x}\, \mathrm{d}\overline{\eta}. \tag{2.9}$$

2.2. *Review of ML's approach*

The crucial assumption embedded in ML's model is that under wave loadings, the shear stress in the mud column decreases monotonically in the vertical direction with the maximum magnitude at the solid bottom, $\eta = 0$. Accordingly, inside the Bingham-plastic mud bed there exists one shear-flow zone ($u_m = u_s(x, \eta, t)$, $0 \leqslant \eta \leqslant \eta_0$) and one plug-flow region ($u_m = u_p(x, t)$, $\eta_0 \leqslant \eta \leqslant d$) with $0 \leqslant \eta_0(x, t) < d$ being the location of the yield surface. We remark here that the terminology of plug flow in both ML and the present analysis is referred to the flow region where the horizontal velocity component is uniform in the vertical extent, but not necessarily invariant laterally. More rigorously, the constitutive equations, (1.1) and (1.2), are actually the leading-order approximation since the contribution from $\partial u_m/\partial x$, which is negligible as shown in the horizontal momentum equation, (2.4), has been ignored. Detailed discussions on the validation of this approximate rheology curve can be found in Balmforth & Craster (1999). By further assuming that the plug-flow region occupies most of the mud column and employing the Kármán momentum integral method along with a prescribed parabolic mud flow velocity profile, ML obtained the explicit form for the plug-flow velocity, u_p,

$$\frac{\partial u_p}{\partial t} \approx \gamma \frac{\partial u_b}{\partial t} + \frac{-\tau_o \mathrm{sgn}(u_p)}{d}, \quad \eta_0 \leqslant \eta \leqslant d, \tag{2.10}$$

and an ordinary differential equation for the location of the yield surface, η_0,

$$u_p \frac{\partial \eta_0^2}{\partial t} + \left(6\gamma \frac{\partial u_b}{\partial t} - 4\frac{\partial u_p}{\partial t}\right)\eta_0^2 - 12u_p = 0. \tag{2.11}$$

Based on ML's model, the anticipated Bingham-plastic mud motions under a surface solitary-wave loading are sketched in figure 1. In this figure the yield surface location, $\eta = \eta_0$, is designated as η_1 when the mud flow moves in the direction of wave propagation (from the left to the right) and $\eta_0 = \eta_3$ when it moves in the opposite direction. Before the arrival of the solitary wave, the entire mud column behaves like a solid and is at rest. As shown in phase 1 of figure 1, a shear-flow layer begins to

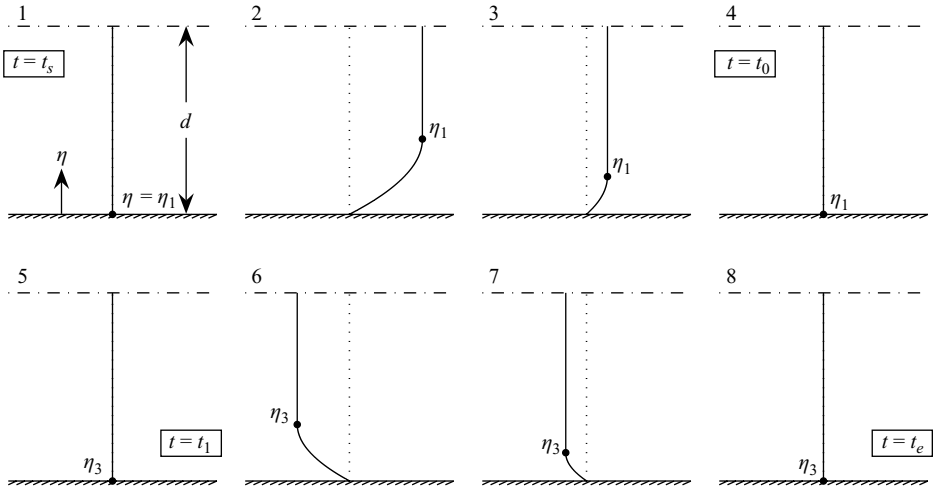

FIGURE 1. Sketches of vertical profiles of horizontal velocity, u_m, inside the mud bed under a surface solitary-wave loading (ML's model and the two-layer scenario). All dots represent the locations of yield surface ($\eta_0 = \eta_1$ for the positive mud motion and $\eta_0 = \eta_3$ for the backward mud motion), dashed-dotted lines denote the water–mud interface and dotted vertical lines are the zero velocity reference. A shear-flow layer develops when the bottom shear stress reaches the yield stress at $t = t_s$ (cf. phase 1). Both mud velocity and the thickness of the shear-flow region first grow and then decrease as shown in phases 2 to 4. The mud motion pauses at $t = t_0$ and restarts to move backwards at $t = t_1$ (see phases 4 and 5). If $t_1 > t_0$, the mud flow is intermittent (i.e. the mud is at rest for a finite time interval $t_0 < t < t_1$), otherwise it moves continuously. Eventually, the mud motion stops at $t = t_e$ and a cycle of mud motion under a solitary-wave loading is completed. In this example, the velocity profile is always monotonically increasing from zero at the bottom to the plug-flow velocity at the mud–water interface.

develop from the solid bottom at $t = t_s$ when the bottom shear stress $\tau_{mb} = \tau_o$. Clearly, this incipient moment can be calculated as

$$\gamma \frac{\partial u_b}{\partial t} - \frac{\tau_o}{d} = 0, \quad t = t_s, \tag{2.12}$$

representing the balance between the driving pressure gradient, which is also proportional to acceleration of wave motions at the water–mud interface, and the bottom friction that is the same as the yield stress at this moment. Phases 2 to 4 in figure 1 suggest that both the mud velocity and the thickness of the shear-flow layer first grow and then diminish as the magnitude of the driving pressure gradient (or acceleration of wave motions) first increases and then decreases. Eventually, the entire mud column pauses and returns to the solid state at $t = t_0$ (i.e. phase 4 in figure 1). The shear flow starts to move in the opposite direction to the wave propagation when the reversed driving pressure gradient yields the bottom mud again at $t = t_1$ (see phase 5). During the backward mud-flow-motion phases, the characteristics of mud velocity and shear-flow-layer thickness behave very much like those at the forward mud motion phases. Finally, the mud flow ends at $t = t_e$, as shown in phase 8. The transition times t_0, t_1 and $t = t_e$ are yet to be determined. ML suggested that when $t_1 = t_0$, the mud flows continuously whereas the mud motion is intermittent if $t_1 > t_0$

(cf. figure 1). For the intermittent mud flow, t_1 can be calculated by

$$\gamma \frac{\partial u_b}{\partial t} + \frac{\tau_o}{d} = 0, \quad t = t_1. \tag{2.13}$$

The physical representation of (2.13) is similar to that of (2.12) except for the directions of mud flow and driving pressure gradient reverse.

Although ML's model is ground breaking, the simplifications employed prevent it from being applied to more complex flow conditions. For instance, the assumption that the shear-flow-layer thickness is much less than the total mud bed thickness, $d \gg 1$, is not always applicable. Consider a solitary wave propagating over a depth $h_0' = 10$ m with $a_0'/h_0' = (h_0'/l_0')^2 = 0.1$. The Bingham-plastic mud has a thickness of $d' = 0.5$ m and a viscosity three orders of magnitude greater than that of water (i.e. $\alpha l_0' = 0.05$ m); the dimensionless mud thickness is only about $d = 10$. Moreover, it is well-known that for a Newtonian boundary-layer flow under unfavourable pressure gradient, the strain rate at the bottom can become zero and eventually a flow reversal occurs, implying that the vertical variation of the strain rate is no longer monotonic. LC demonstrated that during the decelerating phase of a surface solitary-wave loading, motions inside the viscous fluid mud indeed exhibit the flow reversal behaviour. Under a transient wave loading, because of the occurrence of unfavourable pressure gradients, a multi-layer flow structure inside the Bingham-plastic mud, i.e. alternating layers of plug- and shear-flow regions, can exist. Differing from ML's approach, we seek to provide a general investigation of the responses of a Bingham-plastic muddy sea bed to the surface solitary-wave propagation.

3. Solutions inside a Bingham-plastic mud

Figure 2 illustrates the complete mud responses under a surface solitary-wave loading. During the accelerating phases of solitary wave, 1 and 2 in figure 2, a shear-flow region develops from the solid bottom when the pressure-gradient-generated bottom friction overcomes the yield stress. The corresponding yield surface between the plug-flow and the shear-flow regions is designated as $\eta_1(x, t)$. As the fluid particles under the solitary wave start to decelerate, the unfavourable pressure gradient creates zero strain rate at the bottom, which implies that the lower portion of mud is solidified (plug flow) and a second yield surface, $\eta_2(x, t)$, appears; e.g. 4 in figure 2. The corresponding time instant is denoted as $t = t_1$. In terms of the constitutive curve, (1.1) and (1.2), the development of the bottom plug-flow layer represents the transition during which the bottom shear stress decreases from a positive yield stress to a negative yield stress, $\tau_{mb} = -\tau_o$. As the solitary wave keeps propagating forwards, the newly developed lower plug-flow region grows and the positive (unfavourable) pressure gradient can liquefy the bottom solid mud again when the pressure gradient overcomes the yield stress; i.e. 5 and 6 in figure 2. The third interface between the plug flow and shear-flow regions is denoted as $\eta_3(x, t)$ and the time of its occurrence is marked as $t = t_y$. Consequently, a four-layer structure inside the mud column is formed and a flow reversal occurs as shown in panel 7. The subsequent phases show that the sandwiched shear layer vanishes, i.e. the upper two yield surfaces, η_1 and η_2, merge at $t = t_1$ in panel 8, since the driving (positive) pressure gradient becomes fully favourable again. The sea bed continues to flow with a single yield surface

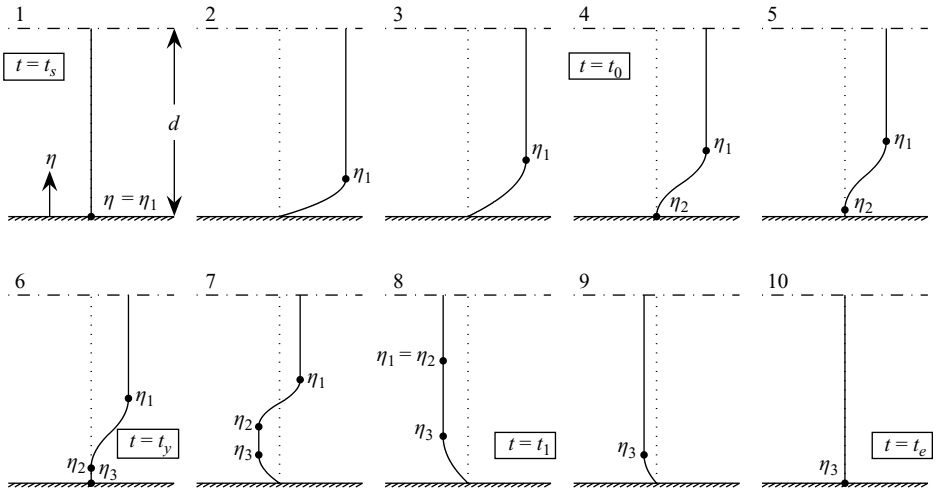

FIGURE 2. Sketches of vertical profiles of horizontal velocity, u_m, inside the mud bed under a surface solitary-wave loading (four-layer scenario). All dots represent the locations of yield surfaces ($\eta_{1,2,3}$), dashed-dotted lines denote the water–mud interface and dotted lines are the zero velocity reference. The mud yields at $t = t_s$ when the bottom shear stress reaches the yield stress. During the beginning phases 1 to 3, there is only one yield surface. In phase 4, a second plug-flow region develops from the solid bottom in response to the unfavourable pressure gradient and the mud plasticity at $t = t_0$ and the new plug-flow layer grows as the strength of the unfavourable pressure gradient increases (cf. phase 5). As the driving unfavourable pressure gradient becomes stronger, the mud in the lower plug-flow region is yielded again at $t = t_y$ in 6. The upper shear layer eventually vanishes, i.e. η_1 and η_2 are merged at $t = t_1$, and the mud motion returns to a single yield surface (η_3) structure. The whole process of mud flow ends at $t = t_e$.

structure as shown in panel 9 and eventually the whole mud column returns to its initial resting state at $t = t_e$. The similar four-layer flow structure (i.e. 7 of figure 2) has also been illustrated by Balmforth, Forterre & Pouliquen (2008) who studied the Bingham-plastic version of the Stokes problem.

In addition to the four-layer and two-layer (ML's model) scenarios, a three-layer scenario is also possible (figure 3). This scenario occurs only if the driving pressure gradient is not strong enough, so the second shear-flow region does not develop and the second plug-flow region will build up until the whole mud column is solidified before the backward mud motions take place (cf. 4 to 6 in figure 3). With this exception, the three-layer scenario is similar to the four-layer scenario: the mud is first liquefied at $t = t_s$, a bottom plug-flow region begins to develop at $t = t_0$, the sandwiched shear layer vanishes at $t = t_1$ and the whole mud motion ends at $t = t_e$. Clearly, the flow reversal does not occur in both three-layer and two-layer scenarios. We reiterate that the two-layer scenario, as shown in figure 1, can only occur when the yield stress is so strong that during the middle phases the entire mud column comes to rest without any bottom plug-flow zone developing (cf. 4 to 5 in figure 1). In addition, there is no presumed shear-flow velocity profile in our two-layer scenario and mud flow must be intermittent (i. e. no mud flow motion during $t_0 \leqslant t \leqslant t_1$). This is very different from ML's model.

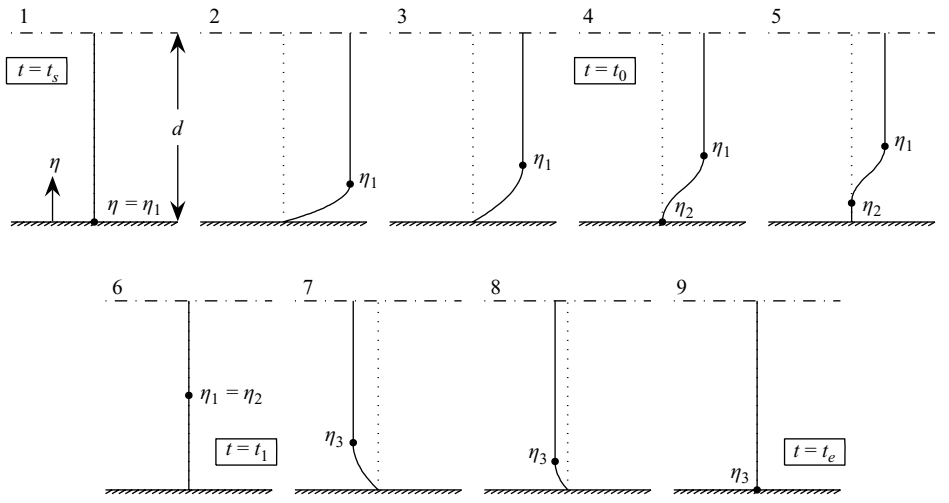

FIGURE 3. Sketches of vertical profiles of horizontal velocity, u_m, inside the mud bed under a surface solitary wave loading (three-layer scenario). All dots represent the yield surfaces ($\eta_{1,2,3}$), dashed-dotted lines denote the water–mud interface and dotted lines are the zero velocity reference. The mud motion is initiated at $t = t_s$ and a second plug-flow region develops from the solid bottom when $t = t_0$. At $t = t_1$, the whole mud column is solidified as the transition between positive plug-flow velocity and the backward movement occurs (cf. phase 6). Thereafter, the mud bed moves backwards with a single yield surface (η_3) structure towards the ending instant, $t = t_e$. To be consistent with the definition in § 3.3, here the notation η_3 denotes the lowest yield surface after η_1 and η_2 have merged. In this example, there is no second, shear-flow layer and flow reversal does not occur.

Based on the above physical pictures, we can now formulate the mathematical model describing Bingham-plastic mud motions under a surface solitary, wave loading within the following framework

I. $t_s \leqslant t \leqslant t_0$: a plug-flow region is on top of a shear-flow region with a single yield surface, η_1 (cf. 1–4 in figure 1; 1–3 in figures 2 and 3);

II. $t_0 \leqslant t \leqslant t_1$: there are multiple yield surfaces with alternating plug–shear–plug–shear–plug–shear flow structure (four-layer scenario: 4–8 in figure 2; three-layer scenario: 4–6 in figure 3) or no mud motion at all (two-layer scenario: 4 and 5 in figure 1);

III. $t_1 \leqslant t \leqslant t_e$: flows return to the plug–shear flow structure with a single yield surface, η_3 (cf. 5–8 in figure 1; 8–10 in figure 2; 7–9 in figure 3).

We note that all the different instants, t_s, t_e, t_0 and t_1, have been illustrated and described in figures 1 to 3. In addition, while for all scenarios t_s has a common definition (see (2.12)), t_0 and t_1 are different for two-layer or three/four-layer scenarios. Both t_0 and t_1 are still parts of the solutions to be determined with the exception that for the two-layer scenario, t_1 has been defined in (2.13).

Despite the possibility of having different multi-layer structures, the momentum equation remains the same in each shear-flow region,

$$\frac{\partial u_s}{\partial t} = \gamma \frac{\partial u_b}{\partial t} + \frac{\partial^2 u_s}{\partial \eta^2}, \tag{3.1}$$

while within the plug-flow layer the momentum equation becomes

$$\frac{\partial u_p}{\partial t} = \gamma \frac{\partial u_b}{\partial t} + \frac{\tau_{pt} - \tau_{pb}}{\kappa_p}, \tag{3.2}$$

where τ_{pt} and τ_{pb} are the shear stresses along the top and bottom of a plug-flow region, respectively, and κ_p is the thickness of this specified layer. However, the boundary and interfacial conditions are not the same for different flow scenarios, which will be described in the following sections.

3.1. *Stage I: initial single yield surface (η_1) structure*

During this initial stage ($t_s \leqslant t \leqslant t_0$), there is only one yield surface, $\eta_1(x, t)$, and the vertical velocity gradient inside the shear-flow layer is always positive, which indicates that plug-flow velocity, $u_{p1}(x, t)$, is non-negative. Therefore, by integrating (3.2) in time we obtain

$$u_{p1}(x, t) = \gamma [u_b(x, t) - u_b(x, t_s)] + \int_{t_s}^{t} \frac{-\tau_o}{d - \eta_1} \, \mathrm{d}\bar{t}, \quad \eta_1 \leqslant \eta \leqslant d. \tag{3.3}$$

As for the shear-flow velocity, we follow the approach of LC and introduce a new variable

$$v_{s1} = u_{s1} - \gamma u_b. \tag{3.4}$$

Thus, the two-point boundary-value problem (BVP) in this region can be expressed in terms of v_{s1} as

$$\frac{\partial v_{s1}}{\partial t} = \frac{\partial^2 v_{s1}}{\partial \eta^2}, \quad 0 \leqslant \eta \leqslant \eta_1, \tag{3.5}$$

with the initial condition

$$v_{s1} = -\gamma u_b, \quad t = t_s, \tag{3.6}$$

and the following boundary conditions

$$\frac{\partial v_{s1}}{\partial \eta} = 0, \quad \eta = \eta_1, \tag{3.7}$$

and

$$v_{s1} = -\gamma u_b, \quad \eta = 0. \tag{3.8}$$

In addition, the continuity of mud flow velocity along the yield surface, $\eta = \eta_1$, must be satisfied. Hence, from (3.3) and (3.4) it is required that

$$v_{s1}(x, \eta_1, t) = -\gamma u_b(x, t_s) - \int_{t_s}^{t} \frac{\tau_o}{d - \eta_1} \, \mathrm{d}\bar{t}. \tag{3.9}$$

The BVP, (3.5) to (3.8), is similar to that derived by LC for a viscous muddy seabed problem. However, the present problem has a moving boundary, i.e. $\eta_1 = \eta_1(x, t)$, which poses a mathematical difficulty in finding an analytical solution. Nevertheless, by adopting the assumption that the thickness of the shear-flow layer is slowly varying in time, $\eta_1(x, t)$ can be approximated as a constant within a small time interval, Δt. Therefore, using the Green's function method (Mei 1995) the solution form can be

obtained as

$$v_{s1}(x,\eta,t)=\int_0^{\eta_1} v_{s1}(x,\xi,t^*)G(\eta,\xi,\Delta t)\,\mathrm{d}\xi-\gamma\int_0^{\Delta t} u_b(x,t^*+\bar{t})\frac{\partial G}{\partial\xi}(\eta,0,\Delta t-\bar{t})\,\mathrm{d}\bar{t}, \tag{3.10}$$

where

$$G(\eta,\xi,t)=\sum_{n=-\infty}^{\infty}\frac{(-1)^n}{2\sqrt{\pi t}}\left\{\exp\left[\frac{-(\eta-\xi+2n\eta_1)^2}{4t}\right]-\exp\left[\frac{-(\eta+\xi+2n\eta_1)^2}{4t}\right]\right\}, \tag{3.11}$$

and $0<\Delta t=t-t^*\ll 1$ in order to satisfy the slowly varying assumption, $\eta_1=\eta_1(x,t)$ from t^* to t. When $t^*=t_s$, the solution becomes

$$\begin{aligned}v_{s1}(x,\eta,t)=\gamma u_b(x,t_s)\sum_{n=0}^{\infty}\sum_{m=-1}^{1}(-1)^{n+m}\left(1-\frac{|m|}{2}\right)\operatorname{erfc}\left[\frac{\eta+(2n+m)\eta_1}{\sqrt{4\Delta t}}\right]\\ -\frac{\gamma}{2\sqrt{\pi}}\sum_{n=-\infty}^{\infty}(-1)^n(\eta+2n\eta_1)\int_0^{\Delta t}\frac{u_b(x,t_s+\bar{t})}{\sqrt{(\Delta t-\bar{t})^3}}\exp\left[-\frac{(\eta+2n\eta_1)^2}{4(\Delta t-\bar{t})}\right]\mathrm{d}\bar{t},\end{aligned} \tag{3.12}$$

with $\eta_1=\eta_1(x,t_s+\Delta t)$. Based on (3.12), it is possible to formulate the general expression for $v_{s1}(x,\xi,t^*)$ in (3.10), which involves a multiple series. However, there is no obvious computational benefit for doing so since the integrals in (3.10) still have to be evaluated numerically. In summary, when the properties of the Bingham-plastic mud and the velocity of water along the water–mud interface, u_b, are given, the thickness of the shear-flow layer, η_1, can be calculated numerically from (3.9). Once η_1 is known, the velocities of the plug flow and shear flow can be obtained by (3.3) and (3.10), respectively. We remark that the current stage ends at $t=t_0$. For a two-layer scenario, t_0 indicates the moment that mud motion pauses from the forward motion whereas in the three/four-layer scenario it represents the instant that zero shear strain rate appears at the solid bottom (see figures 1 to 3).

3.2. *Stage II: multiple yield surfaces structure for a three/four-layer scenario*

During the unfavourable pressure gradient phase, a multiple yield surface structure is formed when $t_0\leqslant t\leqslant t_1$. As mentioned earlier, the mud bed is stationary during this time interval in the two-layer scenario. Referring to figure 2, the maximum possible number of yield surfaces is three, therefore, the momentum equations for these four layers can be formulated as

$$\frac{\partial u_{p1}}{\partial t}=\gamma\frac{\partial u_b}{\partial t}+\frac{-\tau_o}{d-\eta_1},\quad \eta_1\leqslant\eta\leqslant d, \tag{3.13}$$

$$\frac{\partial u_{s1}}{\partial t}=\gamma\frac{\partial u_b}{\partial t}+\frac{\partial^2 u_{s1}}{\partial\eta^2},\quad \eta_2\leqslant\eta\leqslant\eta_1, \tag{3.14}$$

$$\frac{\partial u_{p2}}{\partial t}=\gamma\frac{\partial u_b}{\partial t}+\frac{2\tau_o}{\eta_2-\eta_3},\quad \eta_3\leqslant\eta\leqslant\eta_2, \tag{3.15}$$

$$\frac{\partial u_{s2}}{\partial t}=\gamma\frac{\partial u_b}{\partial t}+\frac{\partial^2 u_{s2}}{\partial\eta^2},\quad 0\leqslant\eta\leqslant\eta_3, \tag{3.16}$$

where η_1, η_2 and η_3 denote the yield surfaces. The associated interfacial and boundary conditions are

$$u_{p1} = u_{s1}, \quad \eta = \eta_1, \tag{3.17}$$

$$\frac{\partial u_{s1}}{\partial \eta} = 0, \quad \eta = \eta_1 \text{ or } \eta = \eta_2, \tag{3.18}$$

$$u_{s1} = u_{p2}, \quad \eta = \eta_2, \tag{3.19}$$

$$u_{p2} = u_{s2}, \quad \eta = \eta_3, \tag{3.20}$$

$$\frac{\partial u_{s2}}{\partial \eta} = 0, \quad \eta = \eta_3; \quad u_{s2} = 0, \quad \eta = 0. \tag{3.21}$$

An additional yielding criterion for the second shear-flow zone, $0 \leqslant \eta \leqslant \eta_3$, is

$$\eta_3 = u_{s2} = u_{p2} = 0, \quad t < t_y, \tag{3.22}$$

where t_y is illustrated in phase 6 of figure 2 and can be determined by

$$\gamma \frac{\partial u_b}{\partial t} + \frac{2\tau_o}{\eta_2} = 0, \quad t = t_y. \tag{3.23}$$

We reiterate that since η_2 is still part of the unknown solutions, the above criterion must be checked at every time step. For the three-layer scenario, η_3 is always zero in this stage. As for the four-layer scenario, $\eta_3 > 0$ when $t \geqslant t_y$. In both scenarios, the mud motion returns to a single yield surface set-up at $t = t_1$ with $\eta_1 = \eta_2$ when the wave-induced pressure gradient becomes truly favourable again (see 8 of figure 2 and 6 of figure 3).

Following the same solution method as shown in the previous section, the plug-flow velocities can be obtained as

$$u_{p1}(x, t) = u_{p1}(x, t_0) + \gamma [u_b(x, t) - u_b(x, t_0)] + \int_{t_0}^{t} \frac{-\tau_o}{d - \eta_1} \, \mathrm{d}\bar{t}, \tag{3.24}$$

$$u_{p2}(x, t) = \gamma [u_b(x, t) - u_b(x, t_y)] + \int_{t_y}^{t} \frac{2\tau_o}{\eta_2 - \eta_3} \, \mathrm{d}\bar{t}, \quad t > t_y. \tag{3.25}$$

For the upper shear-flow zone, solution form of BVP, (3.14) with (3.18), is

$$v_{s1}(x, \eta, t) = \frac{1}{2\sqrt{\pi \Delta t}} \int_0^{\eta_1 - \eta_2} v_{s1}(x, \xi + \eta_2, t - \Delta t) G_1(\eta, \xi) \, \mathrm{d}\xi, \quad t > t_0, \tag{3.26}$$

where

$$G_1(\eta, \xi) = \sum_{n=-\infty}^{\infty} \sum_{m=1}^{2} \exp\left[-\left(\frac{\eta + (-1)^m \xi + 2n(\eta_1 - \eta_2)}{2\sqrt{\Delta t}} \right)^2 \right], \tag{3.27}$$

and $v_{s1} = u_{s1} - \gamma u_b$. We reiterate that Δt should be small in order to satisfy the assumption of slowly varying yield surfaces. In addition, the initial condition, $v_{s1} = v_{s1}(x, \eta, t_0)$, mudt be computed from (3.10). Similarly, for the second shear-flow layer, i.e. (3.16) with (3.21), we obtain

$$v_{s2}(x, \eta, t = t^* + \Delta t) = \int_0^{\eta_3} v_{s2}(x, \xi, t^*) G_2(\eta, \xi, \Delta t) \, \mathrm{d}\xi$$

$$- \gamma \int_0^{\Delta t} u_b(x, t^* + \bar{t}) \frac{\partial G_2}{\partial \xi}(\eta, 0, \Delta t - \bar{t}) \mathrm{d}\bar{t}, \quad t^* \geqslant t_y, \tag{3.28}$$

where $G_2(\eta, \xi, t)$ is the same as G given in (3.11), except for η_1 being replaced by η_3. Recall that the initial condition for this region should be

$$u_{s2} = \gamma u_b + v_{s2} = 0, \quad t = t_y. \tag{3.29}$$

So far, the thicknesses of each layer remain unknown. Three interfacial conditions, (3.17), (3.19) and (3.20), are applied to obtain these variables. Therefore, at every instant we must solve numerically a nonlinear system that involves three unknowns.

3.3. *Stage III: single yield surface (η_3) structure with negative plug-flow velocity*

During this final period ($t_1 \leqslant t \leqslant t_e$), the solutions are very similar to those in stage I. Therefore, we can easily obtain

$$u_{p1}(x, t) = u_{p1}(x, t_1) + \gamma [u_b(x, t) - u_b(x, t_1)] + \int_{t_1}^{t} \frac{\tau_o}{d - \eta_3} \, \mathrm{d}\bar{t}, \tag{3.30}$$

and

$$v_{s2}(x, \eta, t = t^* + \Delta t) = \int_0^{\eta_3} v_{s2}(x, \xi, t^*) G_2(\eta, \xi, \Delta t) \, \mathrm{d}\xi$$

$$- \gamma \int_0^{\Delta t} u_b(x, t^* + \bar{t}) \frac{\partial G_2}{\partial \xi}(\eta, 0, \Delta t - \bar{t}) \mathrm{d}\bar{t}, \quad t^* \geqslant t_1. \tag{3.31}$$

We reiterate that t_1 is part of the solutions from the previous stages and the location of the yield surface, η_3, can be obtained by requiring

$$v_{s2}(x, \eta_3, t) = u_{p1}(x, t_1) - \gamma u_b(x, t_1) + \int_{t_1}^{t} \frac{\tau_o}{d - \eta_3} \, \mathrm{d}\bar{t}. \tag{3.32}$$

All solutions must be carried out until u_{p1} vanishes at $t = t_e$, which completes the process of Bingham-plastic mud response under a surface solitary-wave loading.

3.4. *Examples*

In this section, we present numerical solutions for Bingham-plastic mud motions under a surface solitary-wave loading for different scenarios. The prescribed water velocity along the water–mud interface is assumed to be the undisturbed solitary wave given as

$$u_b(x, t) = \operatorname{sech}^2 \left[\frac{\sqrt{3\epsilon}}{2\mu} (x - x_o - Ct) \right], \tag{3.33}$$

where x_o is the initial position of the wave crest and $C = \sqrt{1 + \epsilon}$ represents the dimensionless celerity. The new parameter $\mu = h_0'/l_0'$ measures the frequency dispersion. In all cases presented here, the following wave parameters are used

$$x = 0, \quad x_o = -50, \quad \epsilon = \mu^2 = 0.1.$$

As for other physical parameters, we shall consider the following example

$$d = 10, \quad \gamma = 0.7, \quad \alpha = 3 \times 10^{-3}, \quad \tau_o = 0.2.$$

In terms of dimensional values

$$h_0' = 10 \text{ m}, \quad a_0' = 1 \text{ m}, \quad \lambda_0' = 200 \text{ m},$$

$$d' = 0.95 \text{ m}, \quad \rho_m = 1.43 \text{ g cm}^{-3}, \quad \nu_m = 3 \times 10^{-3} \text{ m}^2 \text{ s}^{-1}, \quad \tau_o' = 8.67 \text{ N m}^{-2},$$

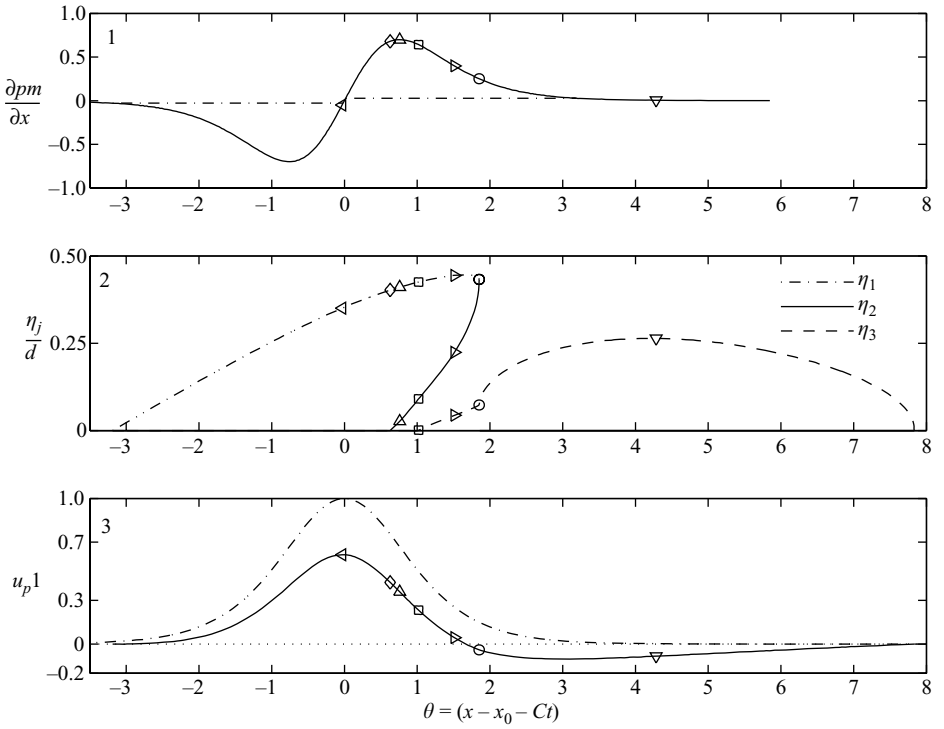

FIGURE 4. Muddy sea bed responses under a surface solitary wave loading (four-layer scenario) at different phases: ◁, (*a*) $\theta = -(x - x_0 - Ct) = -0.032$; ◇, (*b*) 0.629; △, (*c*) 0.760; □, (*d*) 1.019; ▷, (*e*) 1.511; ○, (*f*) 1.851; ▽, (*g*) 4.284. $\gamma = 0.7$, $\tau_0 = 0.2$, $d = 10$. 1. The pressure gradient (dashed-dotted line indicates the yield stress, $\tau_o/(\gamma d)$). 2. Locations of yield surfaces, η_j, $j = 1, 2, 3$. 3. Water–mud interfacial plug-flow velocity, u_{p1} (dashed-dotted line is the water particle velocity at the water–mud interface, u_b). The corresponding velocity profiles are illustrated in figure 5. A second plug-flow region develops after phase (*b*) which is yielded again at (*d*). The mud flow motion returns to a single yield surface (η_3) structure as η_1 and η_2 are merged at phase (*f*).

where $\lambda_0' \approx 2\pi l_0'$ has been defined as the effective wavelength. We remark that $\alpha l_0'$ can be viewed as the boundary-layer thickness based on the Bingham-plastic viscosity. As mentioned in Mei *et al.* (2001), the properties of mud vary widely, depending on the chemical composition, sediment concentration, salinity and other factors. For instance, the mud found in Yunan Province, China has a viscosity three orders of magnitude greater than that of water and the yield stress reaches $O(100)\,\mathrm{N\,m^{-2}}$. On the other hand, Krone (1963) reported that the mud in San Francisco Bay, USA has a viscosity which is of the same order of magnitude as the water and the yield stress is much smaller compared to the mud observed in China. The parameter set employed here is within the range of Provins clay data collected by ML.

In figures 4 and 5 (four-layer scenario), figures 6 and 7 (three-layer scenario) and figures 8 and 9 (two-layer scenario), we demonstrate the effects of the yield stress on the resulting mud motions. Three different values of yield stress, $\tau_0 = 0.2, 2.0, 4.0$, are used while all other parameters remain the same. In the case of a relatively small yield stress ($\tau_o = 0.2$), i.e. figures 4 and 5, the four-layer scenario inside the mud column results. From (2.5) and (2.12), it is clear that the dimensionless parameter $\tau_o/(\gamma d)$

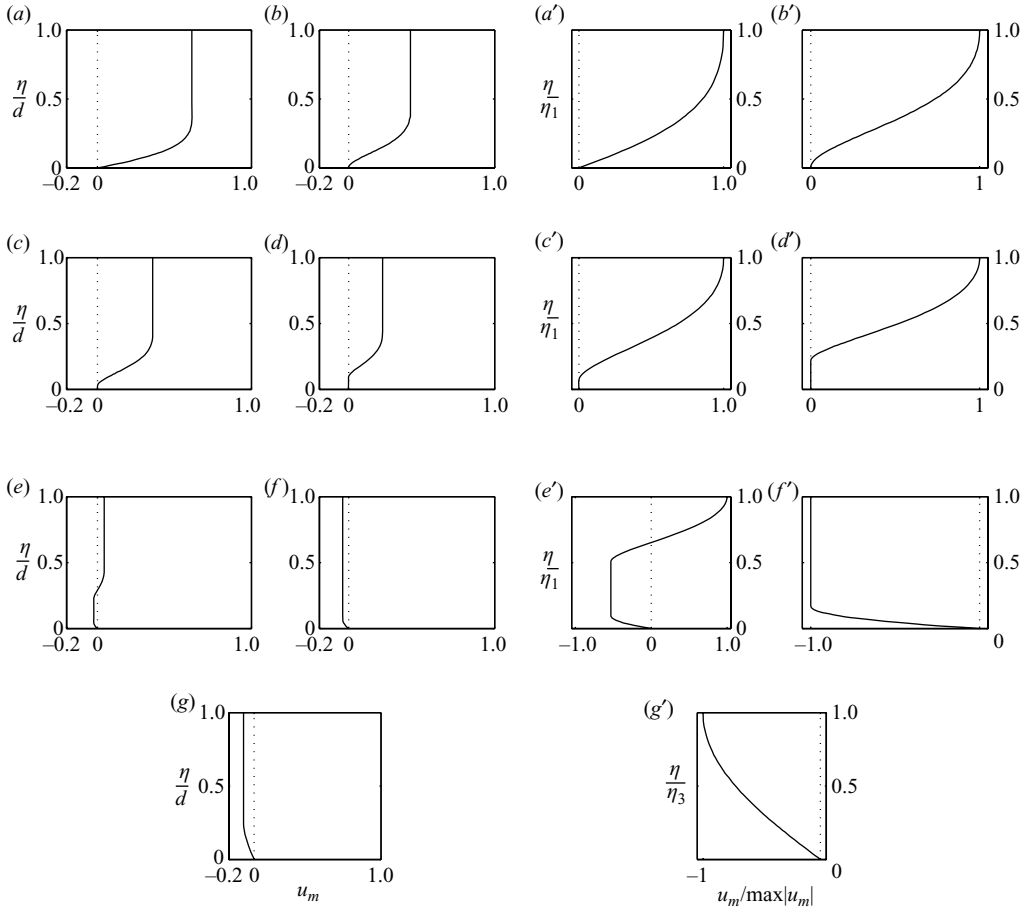

FIGURE 5. Muddy sea bed responses under a surface solitary-wave loading (four-layer scenario) – vertical profiles of horizontal velocity component, u_m, at different phases: (*a*) $\theta = -(x - x_0 - Ct) = -0.032$; (*b*) 0.629; (*c*) 0.760; (*d*) 1.019; (*e*) 1.511; (*f*) 1.851; (*g*) 4.284. (*a*)–(*g*) show the velocities throughout the entire mud column while (*a*′)–(*g*′), are enlargements for $0 < \eta < \eta_1$ or $0 < \eta < \eta_3$ at the same phases. In each plot, the dotted line represents the zero velocity reference line. Clearly, a second plug–shear-flow pair is formed from the solid bottom during the deceleration phase of the surface solitary wave and the flow reversal occurs (cf. phase (*e*)).

measures the relative ease of mobilization of the mud under a given incident wave. As the yield stress is weak relative to the wave loading ($\tau_o/(\gamma d) = 0.029$, see panel 1 in figure 4), the Bingham-plastic mud is quickly liquefied and a shear-flow layer starts to develop from the solid bottom when the friction due to the yield stress is balanced by the pressure force. We note that because of the viscous shear, the plug-flow velocity at the water–mud interface, u_{p1}, is not in phase with the velocity of the solitary wave and the mud flow can move in the opposite direction to wave propagation (see 3 in figure 4). During the initial period ($\theta < -0.032$, phase (*a*)) both the plug-flow velocity, u_{p1}, and thickness of the viscous shear layer, η_1/d, grow in time. The velocity profile at the phase ($\theta = -0.032$) of maximum plug-flow velocity is shown in figure 5(*a*). As the crest of the solitary wave passes, the unfavourable pressure gradient eventually slows

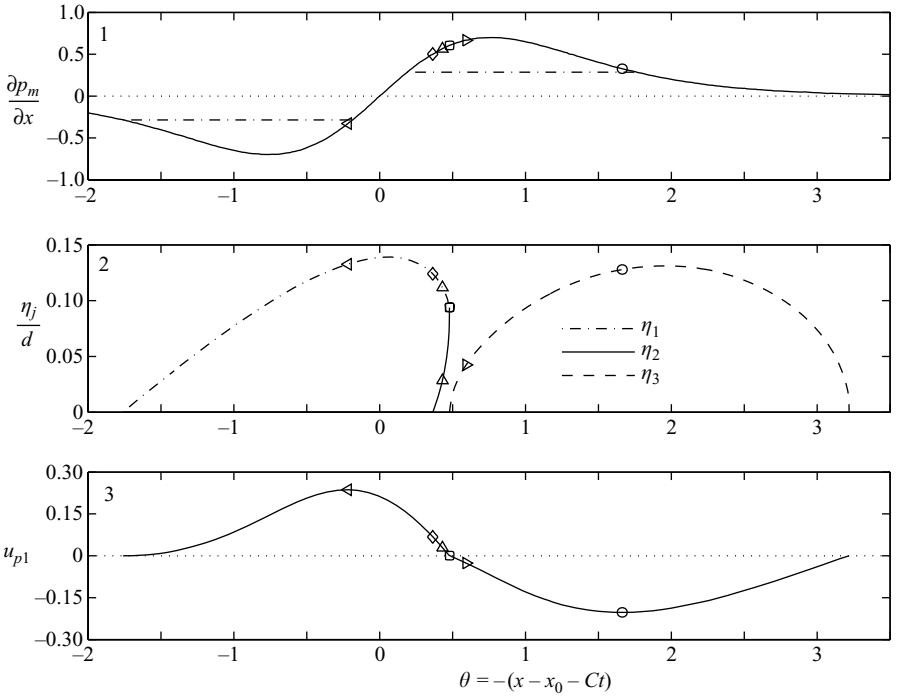

FIGURE 6. Muddy sea bed responses under a surface solitary-wave loading (three-layer scenario) at different phases: ◁, (*a*) $\theta = -(x - x_0 - Ct) = -0.218$; ◇, (*b*) 0.363; △, (*c*) 0.430; □, (*d*) 0.479; ▷, (*e*) 0.594; ○, (*f*) 1.664. $\gamma = 0.7$, $\tau_0 = 2$, $d = 10$. 1. The pressure gradient (dashed-dotted line indicates the yield stress, $\tau_o/(\gamma d)$). 2. Locations of yield surfaces, η_j, $j = 1, 2, 3$. 3. Water–mud interfacial plug-flow velocity, u_{p1}. The corresponding velocity profiles are shown in figure 7. A second plug-flow region develops at phase (*b*), but no flow reversal appears (i.e. at each instant the maximum possible number of yield surface(s) is two). The entire mud column pauses at phase (*d*) and immediately continues the backward motion as a single yield surface structure.

down the forward motion in the mud column as shown in 3 of figure 4. However, the corresponding shear-layer thickness, η_1/d, is still increasing until phase $\theta = 1.658$ (see 2 in figure 4). At the phase $\theta = 0.629$ ($t = t_0$), i.e. figure 5(*b*), the shear strain rate vanishes at the bottom of the muddy bed and the lower most Bingham-plastic mud returns to its plastic state (plug flow). Once the mud is solidified, the friction between the bottom of the mud layer and the solid bed prevents this portion of mud from moving. The material plasticity serves as a resistance to the viscous force. As the unfavourable pressure gradient continues to push the mud column backwards, the thickness of the second plug-flow region (with zero velocity), η_2/d, increases and the shear-flow-layer thickness, $(\eta_1 - \eta_2)/d$, shrinks (cf. phases (*c*) to (*d*) in figures 4 and 5). Since the yield stress is relatively small in this case, as the unfavourable pressure gradient persists, the bottom plug-flow region is eventually yielded again. A new shear layer is formed at $\theta = 1.019$ (i.e. phase (*d*), $t = t_y$) and continues to grow (see (*d*) to (*e*) in figures 4 and 5). At this point, there are two plug-flow regions ($\eta_1 < \eta < d$; $\eta_3 < \eta < \eta_2$) and two shear-flow layers ($\eta_2 < \eta < \eta_1$; $\eta < \eta_3$); the two plug-flow regions move in the opposite direction and flow reversal occurs (cf. (*e*), figure 5). The process continues as the lower shear-flow layer grows and the middle shear-flow layer shrinks.

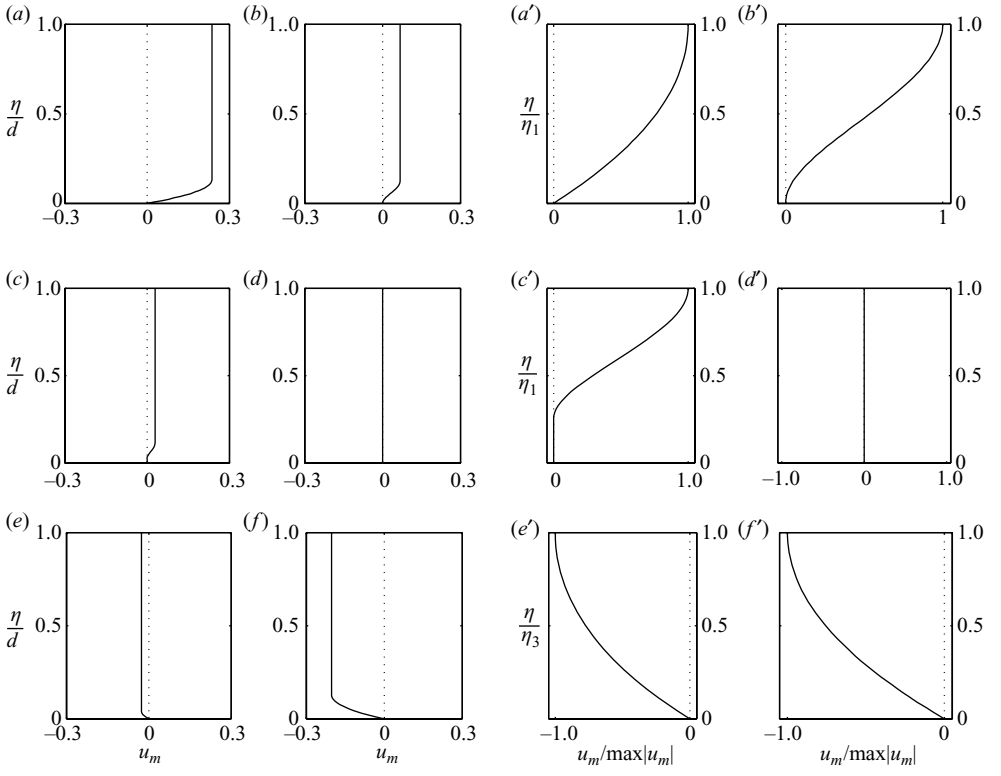

FIGURE 7. Muddy sea bed responses under a surface solitary wave loading (three-layer scenario) – profiles of horizontal velocity component, u_m, at different phases: (*a*) $\theta = -(x - x_0 - Ct) = -0.218$; (*b*) 0.363; (*c*) 0.430; (*d*) 0.479; (*e*) 0.594; (*f*) 1.664. (*a*)–(*f*) show the velocities throughout the entire mud column while (*a*′)–(*f*′) are the detailed features at the same instants. In each plot, the dotted line indicates the zero velocity reference. Because of the strong effect of plasticity, a plug-flow region builds up from the solid bottom and eventually pauses the mud flow at the transition between forward and backward mud motion (see (*b*) to (*d*)). As a result, it is impossible for the flow reversal to develop. When the sea bed begins to move in the opposite direction to the solitary-wave propagation, the mud column can be described again by a single yield surface structure.

Finally, the sandwiched shear layer vanishes at $\theta = 1.851$ (i.e. phase (*f*), $t = t_1$) and the mud motion returns to a single yield surface structure moving towards the end of the event at $\theta = 7.833$ ($t = t_e$). We notice that when the wave crest already propagated far away, i.e. $u_b \approx 0$ or pressure gradient vanishes (see 3 in figure 4), it is actually the inertia of the mud that drives its motion. We remark that the flow reversal, as shown in figure 5(*e*), is also found in the Newtonian fluid mud problem studied by LC (see figure 1 (*c*) in LC). However, the fundamental difference between these two cases is that there is no plug flow in the Newtonian fluid mud problem.

For the case with a larger yield stress ($\tau_0 = 2.0$, figures 6 and 7), it requires a stronger driving pressure gradient to yield the mud and to create the first shear-flow-layer (cf. 1 in figure 6). The shear-flow-layer thickness is also relatively thinner than that in the previous case. During the unfavourable (positive) pressure gradient period, for instance figure 6(*c*), the strong plasticity suppresses the viscous force and the pressure gradient. As a result, the bottom solid layer (plug flow) builds

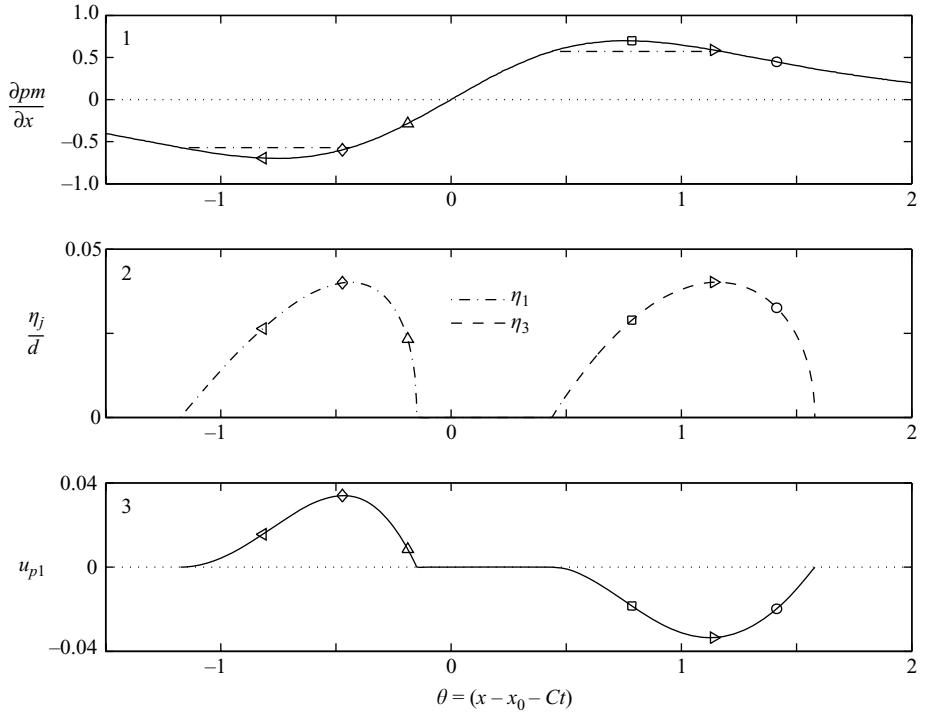

FIGURE 8. Muddy sea bed responses under a surface solitary wave loading (two-layer scenario) at different phases: ◁, (*a*) $\theta = -(x - x_0 - Ct) = -0.818$; ◇, (*b*) −0.471; △, (*c*) −0.188; □, (*d*) 0.784; ▷, (*e*) 1.141; ◯, (*f*) 1.413. $\gamma = 0.7$, $\tau_0 = 4$, $d = 10$. 1. The pressure gradient (dashed-dotted line indicates the yield stress, $\tau_o/(\gamma d)$). 2. Locations of yield surfaces, η_j, $j = 1, 3$. 3. Water–mud interfacial plug-flow velocity, u_{p1}. The corresponding velocity profiles are illustrated in figure 9. In this case, the shear-flow region is relatively small owing to the large yield stress. The mud flow motion pauses for a long interval before it starts to move backwards. Only a single yield surface structure appears throughout the whole process.

up and eventually the mud motion pauses (cf. figure 7(*d*)). From phase (*b*) to (*d*), i.e. stage II: $t_0 \leqslant t \leqslant t_1$, there is only one shear-flow layer being sandwiched by two plug-flow regions. Immediately after the zero motion moment, a new shear-flow layer develops from the solid bottom and continues to grow as the positive pressure gradient increases, see phases (*e*) and (*f*) in figures 6 and 7. The mud flow structure now returns to a single yield surface structure progressing towards the end of the whole process. We reiterate that there is no flow reversal in this case and mud flow motion is continuous.

Figures 8 and 9 show a case where the mud has an even stronger yield stress, i.e. $\tau_0 = 4.0$. The sea bed is barely liquefied and the mud flow motion is relatively small with a single yield surface structure throughout the process. Obviously, a flow reversal is impossible in this case. The mud flow moves intermittently with no motion in the range $-0.149 \leqslant \theta \leqslant 0.438$ ($t_0 \leqslant t \leqslant t_1$, t_1 given in (2.13)). Although we have demonstrated that our results can have very different features from the approach of ML for low yield stress situations (cf. figures 4 to 7), the solutions of this high yield stress case ($\tau_0 = 4.0$) are indeed similar to those presented in ML. Figure 10 shows the locations of yield surfaces and the plug-flow velocity from both studies.

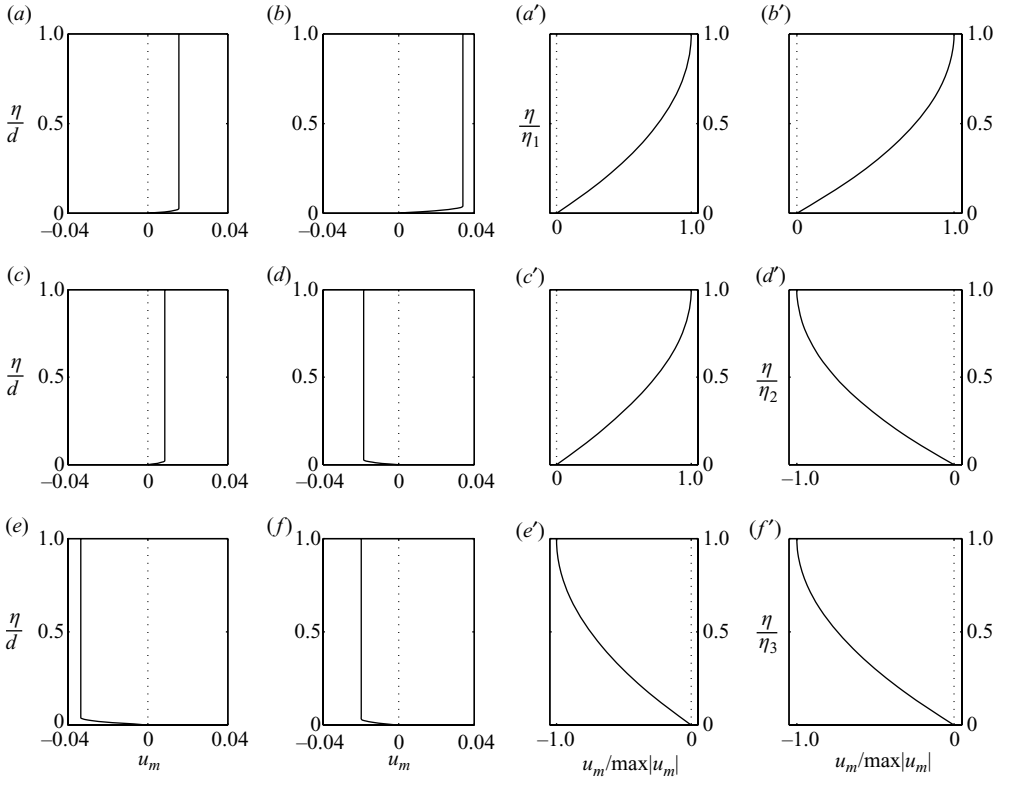

FIGURE 9. Muddy sea bed responses under a surface solitary-wave loading (two-layer scenario) – profiles of horizontal velocity component, u_m, at different phases: (*a*) $\theta = -(x - x_0 - Ct) = -0.818$; (*b*) -0.471; (*c*) -0.188; (*d*) 0.784; (*e*) 1.141; (*f*) 1.413. (*a*)–(*f*) show the velocities throughout the entire mud column while (*a*′)–(*f*′) are the detailed features at the same instants. In each plot, the dotted line indicates the zero velocity reference. The velocity profiles vary monotonically in all phases, which is similar to those presented in ML.

Two models give similar results with some differences. The discrepancy can be mainly attributed to one of ML's assumptions that the shear-flow-layer thickness is small and negligible when computing the plug-flow velocity (see (2.10)). Apparently, this assumption becomes invalid as d decreases.

In figure 11, we show the shear strain rate along the bottom of the muddy bed ($\eta = 0$), $(\partial u_m/\partial \eta)_{mb}$, which is proportional to the bottom shear stress, τ_{mb}. In all three cases, there exists an interval when zero velocity gradient appears along the solid bottom, i.e., $|\tau_{mb}| \leqslant \tau_o$. As shown before, for the large yield stress case, $\tau_0 = 4.0$ (figures 8 and 9), within this period the entire mud column is solidified and remains at rest, while for the other two cases the upper portion of the mud column keeps moving. Therefore, there is no clear trend describing the length of the zero strain rate interval as the physical processes are quite different for each case. The mud movement appears to start and end more gradually for the case of smaller yield stress, i.e. $\tau_0 = 0.2$. When the yield stress is very low, the mud behaves close to a viscous fluid. However, we remark that for a purely viscous fluid mud, the zero bottom strain rate occurs only at an instant.

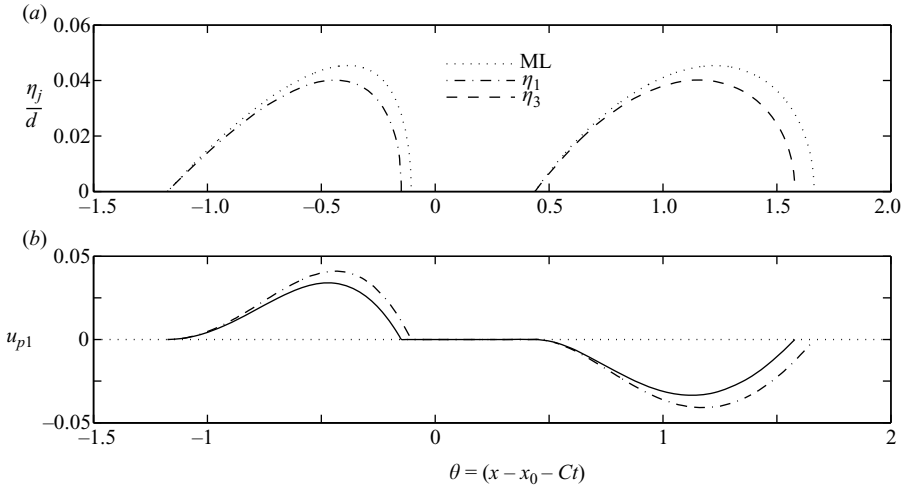

FIGURE 10. Comparison of results from ML and current study for the case of large yield stress, $\tau_0 = 4.0$. (*a*) The locations of yield surfaces (ML: dotted line; current study: dashed-dotted line $= \eta_1$, dashed line $= \eta_3$) and (*b*) is the water–mud interfacial plug-flow velocity (ML: dashed-dotted line; current study: solid line). $r = 0.7$; $d = 10$.

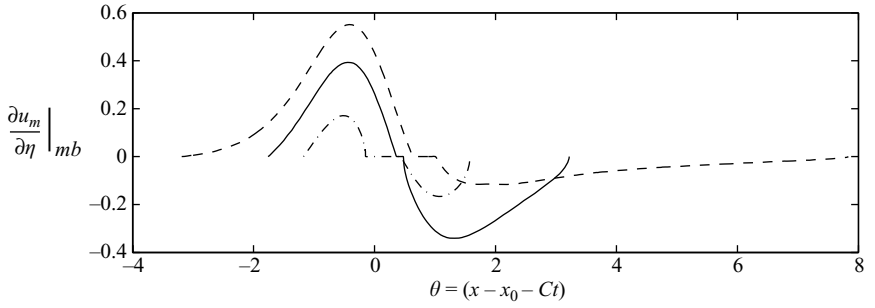

FIGURE 11. The strain rate of various types of mud bed at the bottom. The mud is assumed to have different yield stresses with dashed line, $\tau_o = 0.2$; solid line, $\tau_o = 2.0$; dashed-dotted line, $\tau_o = 4.0$. $r = 0.7$; $d = 10$.

The effect of Bingham-plastic viscosity on the mud flow motion has also been investigated. In figures 12 and 13, we show the plug-flow velocity and locations of yield surfaces for various dimensionless mud-layer thickness, $d = 1$, 5 and 10, with the same initiation parameter: $\tau_0/(\gamma d) = 0.029$ in figure 12 and 0.29 in figure 13, respectively. Since

$$\frac{\tau_0}{\gamma d} = \frac{\tau_0'}{d'} \frac{1}{\epsilon \mu \rho_w g}, \tag{3.34}$$

in each figure a different value of d ($= d'/(\alpha l')$, $\alpha^2 \sim \nu_m$) can be interpreted as the result of changing viscosity (i.e. treat τ_0', ρ_m and d' as constants). Despite the fact that the mud flow motion is initiated at the same instant with a fixed $\tau_0/(\gamma d)$, it does not guarantee that the subsequent mud flow motions will be the same. For instance, all three cases display a four-layer scenario when $\tau_0/d = 0.02$ (figure 12), but behave differently for $\tau_0/d = 0.2$ (figure 13). As can be seen, low-viscosity mud (larger d) can

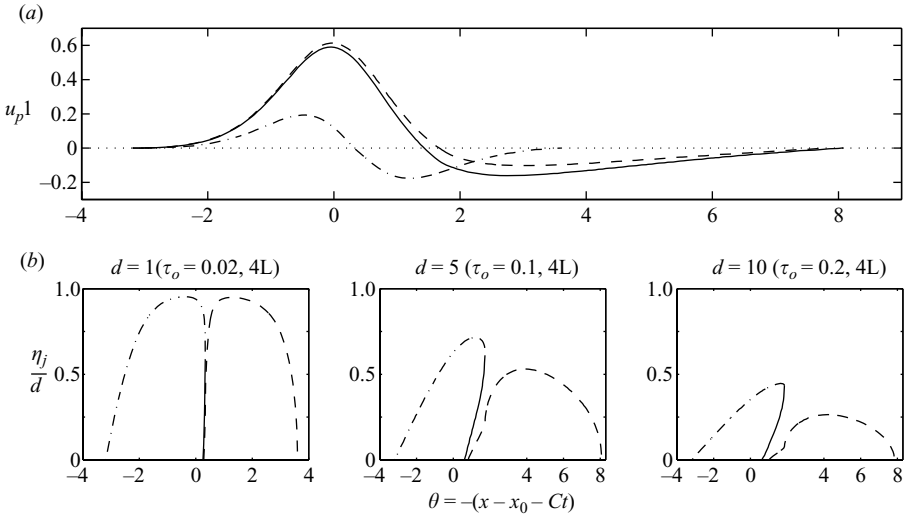

FIGURE 12. Effects of viscosity on the mud flow motion with $\tau_0/d = 0.02$: fixed τ_0/d represents the same τ_0' and d'; small d stands for high viscosity mud. (*a*) The water–mud interfacial plug-flow velocity, u_{p1}, with dashed line: $d = 10$, solid line: 5, dashed-dotted line: 1 and dotted line the zero velocity reference. $\gamma = 0.7$; $\tau_0/d = 0.02$. (*b*) Locations of the yield surfaces, η_j/d, $j = 1, 2, 3$, with dotted line, η_1; solid line, η_2; dashed line, η_3. All three cases display a four-layer scenario and the mud is initiated at the same instant. Low-viscosity mud (larger d) tends to have faster forward plug-flow velocity and the overall mud-flow duration is longer.

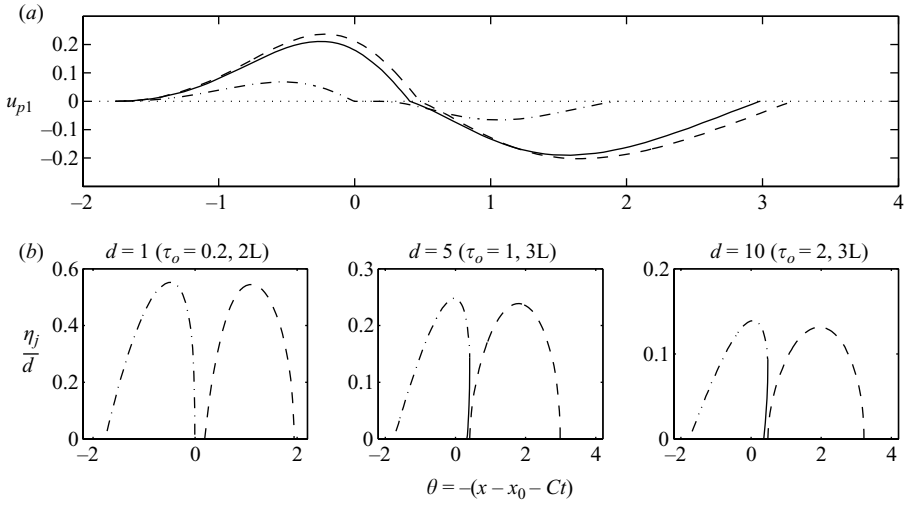

FIGURE 13. Effects of viscosity on the mud flow motion with $\tau_0/d = 0.2$: τ_0' and d' are fixed while a small d corresponds to a high-viscosity mud. (*a*) The water–mud interfacial plug-flow velocity, u_{p1}, with dashed line, $d = 10$; solid line, $d = 5$; dashed-dotted line, $d = 1$. $\gamma = 0.7$; $\tau_0/d = 0.2$. (*b*) Locations of the yield surfaces, η_j/d, $j = 1, 2, 3$, with dotted line, η_1; solid line, η_2; dashed line, η_3. While $d = 1$ (high-viscosity mud) shows a two-layer scenario, the other two are three-layer scenarios.

move faster in the forward direction and the duration of the mud flow motion is longer. In addition, the time interval within which the multiple yield surfaces appear tends to shorten as the viscosity increases (d decreases). However, this does not

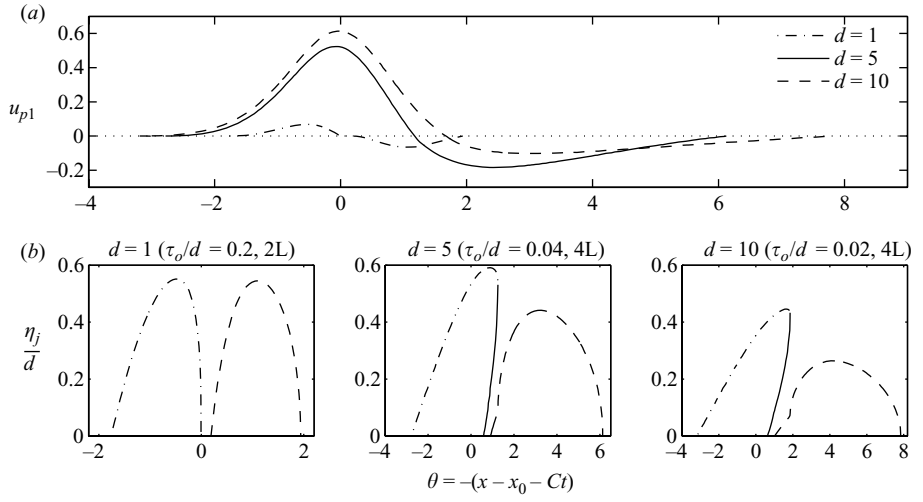

FIGURE 14. Effects of physical mud-layer thickness, d', on the mud-flow motion: a fixed value of τ_0 represents the same viscosity and yield stress (cf. (2.1)). (*a*) The water-mud interfacial plug-flow velocity, u_{p1}, with dashed line: $d = 10$, solid line: $d = 5$, dashed-dotted line: $d = 1$ and dotted line the zero velocity reference. $\gamma = 0.7$, $\tau_0 = 0.2$. (*b*) Locations of the yield surfaces, η_j/d, $j = 1, 2, 3$, with dotted line: η_1, solid line: η_2 and dashed line: η_3. For a thinner sea bed, $d = 1$, the mud-flow motion shows a two-layer scenario while thicker mud cases are four-layer scenarios.

imply that ML's single yield surface model is adequate when the multi-layer interval becomes small (e.g. $d = 1$ in figure 12) as the mud flow behaves very differently, i.e. flow reversal occurs, within this period.

We next examine the effects of the actual mud-layer thickness, d'. In figure 14, the mud column is thicker for larger d since all other physical parameters are kept the same (see (2.1), constant τ_0 and γ are equivalent to fix τ_0' and ν_m). We see that the thin mud-layer case, $d = 1$, has a much smaller plug-flow velocity as the relative yield stress, τ_0/d, is stronger. Referring to figures 4 to 9 (various yield stress, τ_0), we can conclude that the mud bed thickness and strength of yield stress show similar effects on the mud-flow motion: low τ_0/d cases are easier to initiate and tend to have a multi-layer mud structure, stronger plug-flow velocity and a thicker shear-flow region.

As can be seen in figures 4 to 9, the asymmetry of interfacial mud-flow velocity, u_{p1}, suggests that in the light of Eulerian description, the particle orbit of mud is not closed. As a solitary wave described in (3.33) passes by, water particles undergo a forward shift

$$\Delta_w = \int_{-\infty}^{\infty} u_b \mathrm{d}t = \frac{4}{\sqrt{3}} \frac{\mu}{C\sqrt{\epsilon}}. \tag{3.35}$$

By simply integrating over time, along the water–mud interface the net mud movement is $\Delta_m/\Delta_w = 0.357, -0.033, -0.002$ for the cases in figures 4 to 9, respectively. These results reveal that the wave loading could impose an opposite net movement on the Bingham-plastic mud and as the mud becomes stiffer the magnitude of the net movement almost vanishes. The above statement can by no means be referred to the mass transport rate.

3.5. *Wave damping*

Estimating wave energy dissipation in the muddy sea bed and the corresponding wave damping rate is a key objective in studying the interaction between waves and seafloor. Referring to Dalrymple & Liu (1978) and ML, in a moving coordinate following the wave propagation the balance of wave energy requires

$$\frac{\mathrm{d}E'}{\mathrm{d}t'} = -D'_m, \tag{3.36}$$

where E' and D'_m represent the wave energy and the energy dissipation in the muddy sea bed, respectively. The dissipation in (3.36) can be calculated by

$$D'_m = \int_{-\infty}^{\infty}\int_{-d'}^{0} \tau'_m \frac{\partial u'_m}{\partial z'}\,\mathrm{d}z'\,\mathrm{d}x'. \tag{3.37}$$

For a solitary wave, the dimensionless free-surface profile, $\zeta(x,t)$, can be expressed in the form

$$\zeta = \frac{\zeta'}{a'_0} = a\,\mathrm{sech}^2\left[\frac{\sqrt{3\epsilon a}}{2\mu}(x - x_o - \sqrt{1+\epsilon a}\,t)\right], \tag{3.38}$$

where $a = a'/a'_0 \leqslant 1$ is the dimensionless wave height and recall that $\epsilon = a'_0/h'_0$. Therefore, the total wave energy for a solitary wave, i.e. sum of the potential (E'_p) and kinetic (E'_k) energies, can be obtained as

$$E' = E'_p + E'_k, \tag{3.39}$$

where

$$E'_p = \int_{-\infty}^{\infty} \tfrac{1}{2}\rho_w g \zeta'^2 \mathrm{d}x' = \frac{4}{3\sqrt{3}}\rho_w g\,(a'h'_0)^{3/2}, \tag{3.40}$$

and

$$E'_k = \int_{-\infty}^{\infty} \tfrac{1}{2}\rho_w (h'_0 + \zeta')u'^2_b \mathrm{d}x' = (1 + 0.8\epsilon a)E'_p. \tag{3.41}$$

If nonlinearity is weak, i.e. ϵ is small, we can assume $E'_k \approx E'_p$. In addition, for long waves, the celerity is roughly equal to group velocity, $C' \approx C'_g$, which means

$$\frac{\mathrm{d}E'}{\mathrm{d}t'} = C'_g \frac{\mathrm{d}E'}{\mathrm{d}x'} \approx C' \frac{\mathrm{d}E'}{\mathrm{d}x'}. \tag{3.42}$$

Substituting (3.37) and (3.39) into (3.42) into (3.36), we derive the evolution equation of dimensionless wave height

$$\frac{\mathrm{d}a}{\mathrm{d}x} = -\left(\frac{\alpha\sqrt{\epsilon}}{\gamma\mu^2}\frac{\sqrt{3}}{4}\right)\frac{1}{\sqrt{a}}\int_{-\infty}^{\infty}\int_{0}^{d} \tau_m \frac{\partial u_m}{\partial \eta}\mathrm{d}\eta\mathrm{d}x = -\left(\frac{\alpha\sqrt{\epsilon}}{\gamma\mu^2}\frac{\sqrt{3}}{4}\right)\frac{F_D}{\sqrt{a}}, \tag{3.43}$$

where F_D, the dissipation function, represents the double-integral term and has to be calculated numerically.

As an example, figure 15 shows the evolution of solitary-wave height (panel II) for the parameter sets employed in figures 4 and 5 (four-layer scenario), figures 6 and 7 (three-layer scenario) and figures 8 and 9 (two-layer scenario), respectively. The corresponding dissipation functions from both the current and ML's models have also been calculated and shown in panel I in the same figure. For the larger yield stress case ($\tau_0 = 4.0$, two-layer scenario), our results fit well with those of ML,

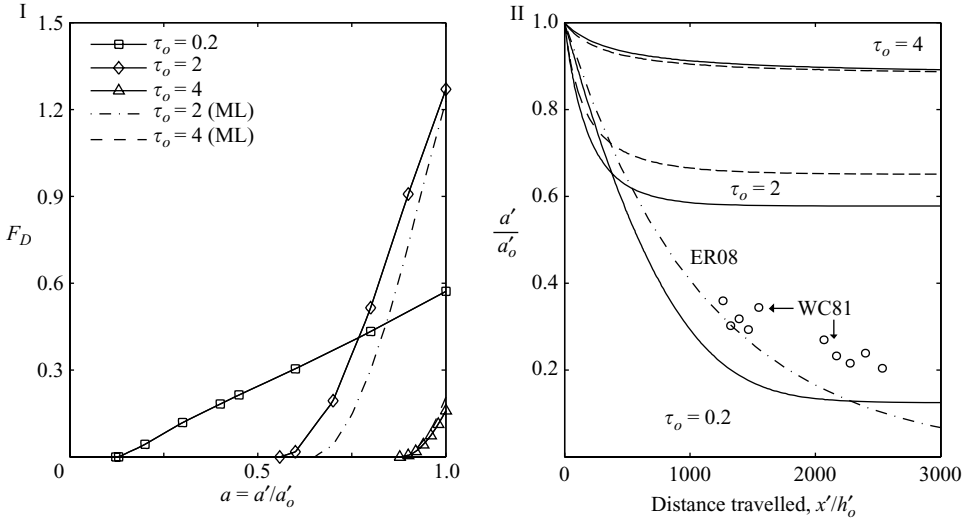

FIGURE 15. I. Dissipation function, F_D (see (3.43)), for $\gamma = 0.7$, $d = 10$ and $\tau_0 = 0.2, 2, 4$. Solid lines are the current results while dashed-dotted and dashed lines are solutions of ML. II. Evolution of dimensionless wave height ($a = a'/a'_0$) with respect to the propagated distance. Solid lines represent the current model results (corresponding to figures 4 to 9 respectively) and dashed lines are the solutions of ML. All circles (WC81) are the field observations of Wells & Coleman (1981) and the dashed-dotted line (ER08) shows the calculation using the measured dissipation rate at 4.5 m deep water by Elgar & Raubenheimer (2008). In our numerical example, we consider a constant water depth, $h'_0 = 10$ m, whereas for WC81 the depth ranges from 7.1 to 8.7 m.

as expected. However, the discrepancy becomes obvious as the strength of the yield stress decreases. Note that we are unable to compare the results for $\tau_0 = 0.2$ (four-layer scenario) since an unbounded shear-layer thickness occurs in ML's model (see figure 4 in ML for more details). In addition, in panel I we observe that there is no clear relationship between the values of F_D and strength of yield stress. In the case with larger τ_0, the corresponding strain rate is weaker. However, the product of strain rate and shear stress, which actually accounts for the energy dissipation, is not necessarily smaller (i.e. F_D can be larger). Referring to panel II, we find that the wave height can be damped out severely by the presence of Bingham-plastic mud. For instance, the case of $\tau_0 = 0.2$ shows that wave height could be reduced by 50 % after it propagates over $x'/h'_0 \sim 600$. Moreover, as can be seen in panel II, both our results and ML's solutions approach asymptotic values (or equivalent to F_D approaching zero in panel I), which means that the attenuated surface solitary wave can no longer move the Bingham-plastic mud as the diminished wave pressure gradient becomes too weak for the mud to yield, i.e. $|\partial u_b/\partial t| - \tau_0/(\gamma d) < 0$. Since mud with weaker yield stress is less able to resist the viscous shearing than that with stronger yield stress, it can eventually dissipate more wave energy.

In figure 15 the field observations by Well & Coleman (1981, WC81: circles) and Elgar & Raubenheimer (2008, ER08: dashed-dotted line) are also plotted in panel II. For Well & Coleman's observations, the water depth at the first station in their experiment (i.e. h_1 in table 1 of Well & Coleman 1981; $h_1 = 7.1 - 8.7$ m) has been used, whereas in Elgar & Raubenheimer's damping curve we adopt a constant depth

of 4.5 m (see figure 2 in Elgar & Raubenheimer 2008). We recall that in our results $x'/h'_0 = x/\mu$ with $\mu = \sqrt{0.1}$ and $h'_0 = 10$ m. As shown in panel II, one of our wave height curves ($\tau_0 = 0.2$) is close to WC81 and ER08. In fact, if we increase the value of τ_0 slightly, the results will fit WC81 very well. However, we do not expect that our present model can fully explain the field observations, as the wave conditions and mud properties in both WC81 and ER08 are incomplete. For instance, the mud in WC81 is inhomogeneous with density, $\rho_m = 1.03 - 1.24\,\mathrm{g\,cm^{-3}}$, and viscosity, $\mu_m = 0.002 - 20\,\mathrm{kg^{-1}\,m\ s^{-1}}$. In addition, the mud-layer thickness is about 0.5 m. Although no yield stress data is available in WC81, the mud is said to exhibit very low strength. For the mud property in ER08, the sea bed has been described as a layer of 0.3 m thick yogurt-like mud above a harder clay bottom. The mud has a density, $\rho_m = 1.3\,\mathrm{g\,cm^{-3}}$, and can resist shear. Despite the fact that the physical parameters in the field studies and the current numerical examples are not perfectly matched, the comparison of wave height attenuation does suggest that the muddy seabeds mentioned in these two sites behave more closely to Bingham-plastic mud with weaker yield stress where ML's model is not adequate for describing the mud-flow motion as the multi-layer scenario occurs.

4. Concluding remarks

Responses of a Bingham-plastic muddy seafloor under a surface solitary-wave loading have been investigated. A semi-analytical/numerical approach is used to obtain solutions inside the mud bed. Our analyses suggest that layered flow structures can occur, depending on the yield stress and the viscosity of the mud, the thickness of the mud bed and the strength of the solitary wave. Four alternating plug-flow and shear-flow layers are possible. The wave damping rate for the solitary wave is also estimated and there are indications that they agree qualitatively with available field data. Although we have successfully demonstrated the detailed mud motions driven by a surface solitary-wave loading, further studies, both analytical and experimental, are required in order to understand better the mud dynamics under more complex water wave loadings, such as cnoidal waves and irregular waves.

This work was supported by the Physical Oceanography Program of National Science Foundation, the Coastal Geosciences Program of the Office of Naval Research and the New York Sea Grant.

REFERENCES

Balmforth, N. J. & Craster, R. V. 1999 A consistent thin-layer theory for Bingham plastics. *J. Non-Newtonian Fluid Mech.* **84**, 65–81.

Balmforth, N. J. & Craster, R. V. 2001 Geophysical aspects of non-Newtonian fluid mechanics. In *Geomorphological Fluid Dynamics* (ed. A. Provencale & N. Balmforth). Lecture Notes in Physics, vol. 582, pp. 34–51. Springer.

Balmforth, N. J., Forterre, Y. & Pouliquen, O. 2008 The viscoplastic Stokes layer. *J. Non-Newtonian Fluid Mech.* in press.

Dalrymple, R. A. & Liu, P. L.-F. 1978 Waves over soft muds: a two layer model. *J. Phys. Oceanogr.* **8**, 1121–1131.

Elgar, S. & Raubenheimer, B. 2008 Wave dissipation by muddy seafloors. *Geophys. Res. Lett.* **35**, L07611, doi:10.1029/2008GL033245.

Forristall, G. Z. & Reece, A. M. 1985 Measurements of wave attenuation due to a soft bottom: the SWAMP experiment. *J. Geophys. Res.* **90**, 3367–3380.

Gade, H. G. 1958 Effects of a non-rigid, impermeable bottom on plane surface waves in shallow water. *J. Mar. Res.* **16**, 61–82.

Healy, T., Wang, Y. & Healy, H.-J. 2002 *Muddy Coasts of the World: Processes, Deposits and Function*. Elsevier.

Krone, R. B. 1963 A study of rheologic properties of estuarial sediments. Tech. Bull. No. 7, Committee on Tidal Hydraulics, U S Army Corps of Engineers.

Liu, P. L.-F., Park, Y. S. & Cowen, E. A. 2007 Boundary layer flow and bed shear stress under a solitary wave. *J. Fluid Mech.* **574**, 449–463.

Liu, P. L.-F. & Chan, I-C. 2007 On long-wave propagation over a fluid-mud seabed. *J. Fluid Mech.* **579**, 467–480.

MacPherson, H. 1980 The attenuation of water waves over a non-rigid bed. *J. Fluid Mech.* **97**, 721–742.

Massel, S. R. 1996 *Ocean Surface Waves: Their Physics and Prediction*. World Scientific.

Mathew, J., Baba, M. & Kurian, N. 1995 Mudbanks of the southwest coast of India I: Wave characteristics. *J. Coastal Res.* **11**, 168–178.

Mei, C. C. 1995 *Mathematical Analysis in Engineering*. Cambridge University Press.

Mei, C. C. & Liu, K.-F. 1987 A Bingham-plastic model for a muddy seabed under long waves. *J. Geophys. Res.* **92**, 14581–14594.

Mei, C. C., Liu, K.-F. & Yuhi, M. 2001 Mud flows – slow and fast. In *Geomorphological Fluid Dynamics* (ed. A. Provencale & N. Balmforth). Lecture Notes in Physics, vol. 582, pp. 548–578. Springer.

Mei, C. C., Stiassnie, M. & Yue, D. K.-P. 2005 *Theory and Applications of Ocean Surface Waves*. World Scientific.

Ng, C.-O. 2000 Water waves over a muddy bed: a two-layer Stokes' boundary layer model. *Coastal Engng.* **40**, 221–242.

Park, Y. S., Liu, P. L.-F. & Clark, S. 2008 Viscous flows in a muddy seabed induced by a solitary wave. *J. Fluid Mech.* **598**, 383–392.

Wells, J. T. & Coleman, J. M. 1981 Physical processes and fine-grained sediment dynamics, coast of Surinam, South America. *J. Sed. Pet.* **51**, 1053–1068.

Winterwerp, J. C., de Graf, R. F., Groeneweg, J. & Luojendijk, A. P. 2007 Modeling of wave damping at Guyana mud coast. *Coastal Engng* **54**, 249–261.